

Research on Calculation Method of Bearing Capacity of Stainless Steel Lipped C-Section Beams in Local Buckling

Meihe Chen^a, Shenggang Fan^a, Zhixia Ding^b, Ganping Shu^a, Baofeng Zheng^a, Qinglin Jiang^c

Key Laboratory of Concrete and Prestressed Concrete Structures of Ministry of Education, School of Civil Engineering, Southeast University, Nanjing, China^(a)

Jiangsu Bosen Architectural Design Co. Ltd, Wuxi, China^(b)

Jiangsu Dongge Stainless Steel Ware Co. Ltd, Dongtai, China^(c)

Abstract

Stainless steel has an attractive appearance and is a recoverable and sustainable material that is widely applied in engineering. To explore the accurate calculation method of the local buckling bearing capacity of stainless steel lipped C-section beams, this paper builds finite element models that are developed with the ABAQUS computer software package verified by experimental results. The models were used to conduct parametric studies on the factors influencing the member strength, which reveal the influence regularity of various factors and yield key factors. Finally, based on the finite element analysis of 238 specimens under major axis bending and 229 beams specimens under weak axis bending, respectively, direct strength equations for major axis bending and weak axis bending lipped C-section stainless steel beams are proposed. Comparison of test results with equation predictions indicates that the formulas have high accuracy and reliability and can accurately calculate the bearing capacity of lipped C-section stainless steel beams.

Keywords

Stainless steel column; Lipped C-section; Local buckling; Calculation method; Direct strength method.

1 Introduction

Stainless steel has traditionally been regarded as an extravagant solution to structural engineering problems. Consequently, the use of stainless steel as a primary structural material for conventional construction remains rather limited. Previously, coupled with the high initial material costs, there have been a number of disincentives to adopt stainless steel, including limited structural design guidance, restricted section availability (and no standardisation) and a lack of understanding of the additional benefits of stainless steel amongst structural engineers. However, currently, with the advent of the entire-life cycle design method of engineering structures, taking into consideration the architectural structure's initial costs and running costs, including maintenance, repair and replacement, the overall cost exhibits a significant downward trend because the material costs have been compensated. This downward trend in overall cost has paved the way for increased use of stainless steel in building structures in recent years.

At present, there are a lot of reports on local buckling in cold-formed thin-walled steel members. Kwon and Hancock (1992) conducted stiffened flange and non-stiffened flange C-section axial compression columns and found that there was no adverse effect between local buckling and distortional buckling modes. Feng and Young (2006, 2007) performed experimental investigations on the high-strength austenitic and duplex stainless steel tubular members subjected to web crippling, and proposed the formula for calculating the web crippling strength. Niu et al. performed tests on 6 I-shaped with lateral constraints and 24 I-beams with non-lateral confinement subjected to pure bending, respectively, and obtained the ultimate bearing capacity and the bearing capacity in the local-global buckling. Liu (2012) conducted local buckling tests and finite element analysis on stainless steel lipped C-section stud columns (under uniform stress and eccentric compression, respectively) and proposed direct strength equations for their design. Zhang (2014) performed experimental distortional buckling and local buckling respectively. According to the tests, the direct strength method for distortional buckling and local buckling capacity are further modified and the accuracy is verified. Yuan (2014) performed experimental and numerical investigations on the local and local-global buckling of I-section and box-section welded stainless steel columns and presented new direct strength methods for design respectively. Hancock and Schafer et al. (2008, 1998, and 2006) proposed the direct strength method to overcome the shortcomings of the effective width.

Above all, existing studies mainly focused on the mechanical properties of closed section stainless steel members. Few studies have been carried out to investigate the bearing capacity of open section members, especially for stainless steel members of lipped C-section. Therefore, This article establish the nonlinear numerical models of stainless steel beams subjected to major axis bending and weak axis bending that use the Python programming language. First, the models were verified by experimental results, and thus they can exactly simulate the mechanical properties of stainless steel lipped C-section beams under bending. Then, the models were used to conduct parametric studies on the factors influencing member strength, which reveal the regularity of various factors' influence on the bearing capacity of beams and identify key factors. Finally, based on the finite element analysis, direct strength equations for stainless steel lipped C-section beams are proposed, which better predict the local buckling capacity of the member under major axial bending and weak axial bending.

2 Specimens

Two groups were simulated: major axis bending and weak axis bending. As shown in Fig. 1, the 3600 mm, four-point major axial bending model, consist of a pair of 4000 mm long C-sections in parallel, loaded at the 1/3 points. The members are oriented in an opposed fashion, such that in-plane rotation of the C-sections leads to tension in the panel, and thus provides additional restriction against distortional buckling of the compression flange. Small angles (60×60×5 mm) are attached to the tension flanges every 360 mm in the constant moment region, and there is one in the shear span separately. Except 2 half-wavelength in the centre of constant moment region, a through-fastened standard steel decking (YX15-225-900) is attached to the compression flanges. Hot-rolled tube sections (150×150×10mm) shown in the Fig. 2, bolt the pair of C-sections together at the load points and the supports, and insure shear and web crippling problems are avoided at these locations.

The appropriate panel-to-section fastener detail for restricting the distortional mode is a pair of high strength bolts placed one-third of flange width, and spaced 225 mm in the constant moment region. In the shear span, screws spaced 112.5 mm.

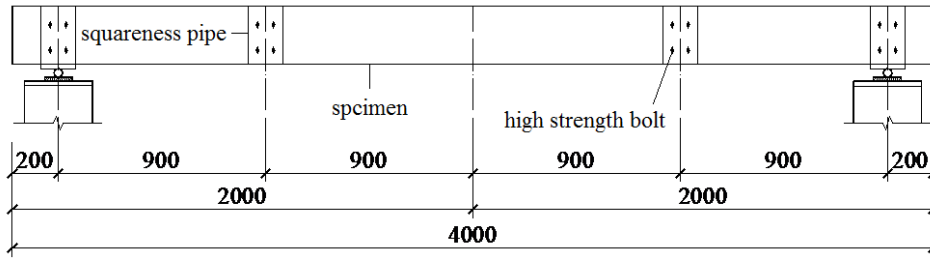


Fig. 1 Model of Specimen.

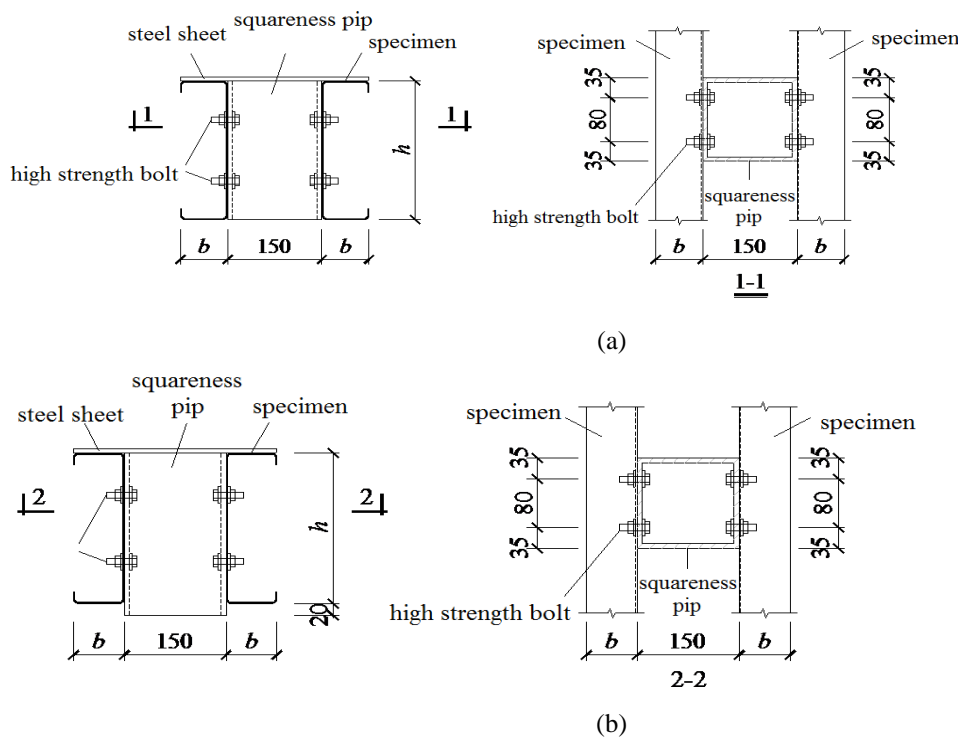


Fig. 2 Hot-rolled tube section (a) Load points, and (b) the supports.

Major axis bending members of lipped C section are selected, with section sizes including C100×50×15×2.0, C150×60×20×2.0, C250×50×20×2.0, C250×75×20×2.0 and C250×75×20×2.5, as detailed in Table 1. Grouping as well as geometric dimensions of weak axis bending members are detailed in Table 2.

Table 1 Group number and dimensions of lipped C section column specimens under major axial bending

Group code	Section code	h/m m	b/m m	a/mm	r/m m	t/mm	Test results P_T/kN	FE result P_{FE}/kN	Deviation	P_{FE}/P_T
SP-1	C150×60×20×2.0	150	60	20	2	2.0	80.11	104.56	30.52%	1.31
SP-2	C250×50×20×2.0	250	50	20	2	2.0	65.86	70.26	6.68%	1.07
SP-3	C250×75×20×2.0	250	75	20	2	2.0	86.77	84.74	-2.34%	0.98
SP-4	C250×75×20×2.5	250	75	20	2	2.5	60.42	61.36	1.56%	1.02
SP-5	C300×80×20×2.0	300	80	20	2	2.0	51.85	54.25	4.63%	1.05
SP-6	C400×90×20×2.0	400	90	20	2	2.0	32.74	31.32	-4.34%	0.96
Average error									3.91%	1.01

Note: r is the fillet radius of the lip; section means height $h \times$ flange width $b \times$ lip with $a \times$ thickness t , and the meanings of symbol h , b , a , t and r are illustrated in Fig. 2. The average error in the table does not contain the result of SP-1 and calculated using the absolute value.

Table 2 Group number and dimensions of lipped C section column specimens under weak axial bending

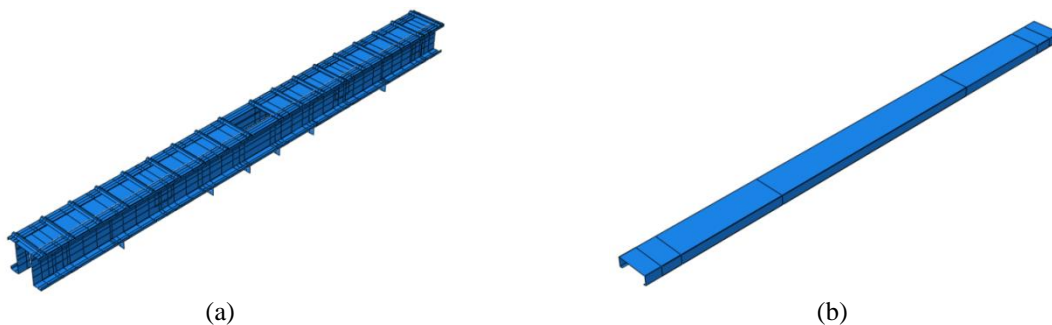
Group number	Section code	h/mm	b/mm	a/mm	r/m m	t/m m	Test results P_T/kN	FE result P_{FE}/kN	Deviation	P_{FE}/P_T
WP-1	C100×50×15×2.0	100	50	15	2	2.0	8.24	8.45	2.54%	1.03
WP-2	C150×60×20×2.0	150	60	20	2	2.0	10.81	10.58	-2.17%	0.98
WP-3	C250×50×20×2.0	250	50	20	2	2.0	7.62	7.75	1.64%	1.02
WP-4	C250×75×20×2.0	250	75	20	2	2.0	3.85	4.18	8.47%	1.08
WP-5	C250×75×20×2.5	250	75	20	2	2.5	5.18	5.47	5.54%	1.06
WP-6	C300×80×20×2.0	300	80	20	2	2.0	3.88	4.02	3.53%	1.04
Average error									3.98%	1.03

3 Finite Element Modelling

Numerical simulation conducted to investigate the failure mode, ultimate capacity and load-displacement of a stainless steel beam. Furthermore, a comparison is made between the numerical results and the test results to verify the accuracy of the finite analysis and the feasibility of the method.

(1) FE model

The finite element software ABAQUS is adapted to build the calculation model of a stainless steel beam. Fig. 3(a) shows the finite element modelling of weak axis bending beam. The finite element modelling of major axis bending beam is shown in Fig. 3(b).

**Fig. 3** Finite element modelling of beams (a) Major axis bend, (b) Weak axis bend.

(2) Material modelling

Since study of the C-sections are the primary research objective, only the C-section is modelled as inelastic, all other components are modelled as linear elastic. Based on the test results of the mechanical properties of stainless steel in this paper, the two-stage stainless steel constitutive model proposed by Gardner (2002) is used to calculate the plate and corner regions in the stainless steel column. The Poisson's ratio μ is set to 0.3 and the elastic moduli E is set to 1.96202 for both the plate section and panel and 1.97029 for the corner section.

(3) Element type

Since the material thickness of cold-formed steel members is thin compared to the element's width, the shell element is appropriate choices. The S4R (4-node, quadrilateral, stress/displacement shell element with reduced integration) shell element was selected for the ABAQUS model of members in this research. The stainless steel sections, panel, and hot-rolled tubes are modelled using S4R shell elements.

(4) Loading method and boundary condition

- Major axis bending

The major axis bending beam is simply supported at the two end tubes. The tube and section connected by tying four nodes of the section to the surface of the tube (to simulate the four bolts). ABAQUS provides a Multi-Point Constraint (MPC in ABAQUS) library for different connection/contact modelling. To simplify the models, the contact and potential friction between the tube and section are ignored in the model. This assumption is also applied to the panel-to-section connector. The panel and section are connected only at the fastener locations via the "Beam" constraint between the corresponding nodes. The steel angle bolted at the bottom flanges of the paired sections are also simulated by the use of "Beam" restraints on these two nodes.

- Weak axis bending

For the weak axis-bending beam, flanges at the support are couple to the reference point via the "Rigid Tie" to ensure the uniform deformation. The constraints are imposed on five DOFs (UX, UY, UZ, ROTY and ROTZ) at one support end, and four DOFs are constrained except for the Z-translational degree (UZ) and X-direction rotational degrees (ROTX) at the other supporting end.

- Geometric Imperfection

Geometric imperfections have a significant effect on the strength and post-buckling behaviour of many C-sections. Therefore, it is necessary and important to consider geometric imperfections in the finite element model. Two methods were proposed by Schafer and Peköz (1998) for calculation geometric imperfections: expression method and probabilistic method. The results of a finite element model with 50% CDF imperfection fit well with the test results (Cheng 2005, Haidarali and Nethercot 2011).

The measured amplitude was adapted in the FE model to simulate the experimental column specimens, while the amplitude of the imperfection in the FE model of parametric analysis is calculated using the first-order elastic buckling mode of the defect distribution model.

4 Finite Element Analysis

To verify the accuracy and feasibility of the finite element model, comparisons were made between the finite element analysis results and the test results in terms of the failure mode, capacity, load-displacement and ultimate capacity.

4.1 Failure modes

For the major axis bending beams, the failure modes of specimens are consistent with the modes observed by the finite element analysis except for SP-1 and SP-2. The local buckling and final failure of the specimen are concentrated in the area of the beam without steel sheet. The main reason is that there is no effective connection between the steel sheets used to restrain the top flange on the SP-1, resulting in the connection of the steel plate joints on the specimen less constrained. Further, the distribution distance of the screw in the pure bending zone of SP-1 was 225mm, which lead to the specimen less constrained. The reason for SP-2 is the latter. Fig. 4 shows a comparison of the test failure mode for SP-3 with the finite element result.

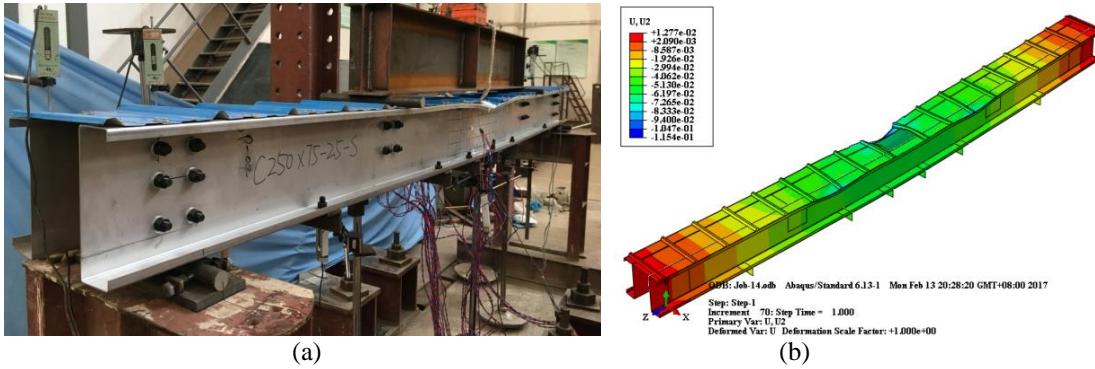


Fig. 4 Comparison of SP-3 failure modes (a) experimental result and (b) FE result.

For the weak axis bending beams, the experimental results of the failure modes of specimen (WP-1 ~ WP-6) are in good agreement with the finite element results that are local buckling occurred at the web in the constant moment region. Fig.5 shows a comparison of the test failure mode for WP-1 with the finite element result.

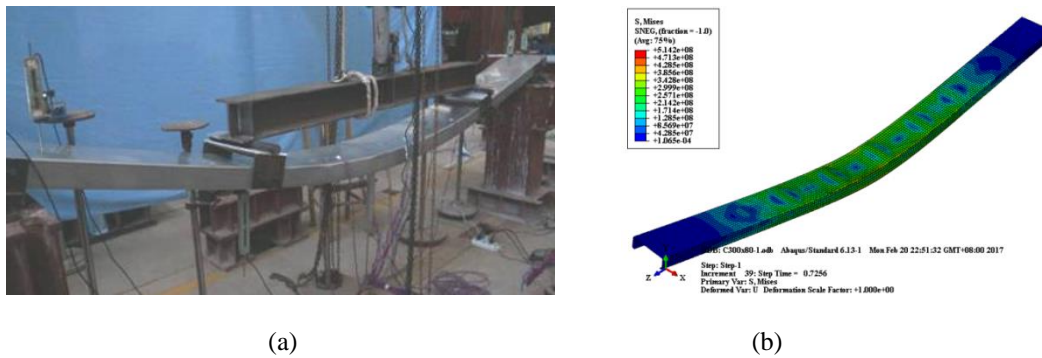


Fig. 5 Comparison of WP-1 failure modes (a) experimental result and (b) FE result.

4.2 Load–displacement curves

Fig. 6 compares numerical load–displacement curves with test curves of major axis bending specimens. FE curves of major axis bending specimen are generally in close agreement with the test, but there is a certain error between the experimental results with FE results of SP-1, mainly due to that SP-1 was the first experimental specimen, with the maximum cross section height and also the biggest difficulty of experiment. Besides, the loading rate was too fast during experiment, so that it's a failure to capture the ultimate bearing capacity data, resulting in directly declining after reaching the maximum value of load-displacement curve and the certain error between FE results.

The experimental and FE load vs. displacement curves for weak axis bending specimens is compared in Fig. 7. FE curves of weak axis bending specimen are generally in close agreement with the test, but there is a certain error between the experimental results with FE results of load–displacement curves of WP-6, mainly due to the effect of loading rate. There is a big difference between FE extreme points and experimental extreme points of load-displacement curves of WP-4 and WP-5. The major reasons are: the effect of specimen weight was ignored but the bearing capacity of the specimen was small so that the proportion of specimen weight processed in the bearing capacity cannot be ignored, and the range of pressure sensor in use is 10 t, but the actually used range is less than one-tenth of that, leading to certain error.

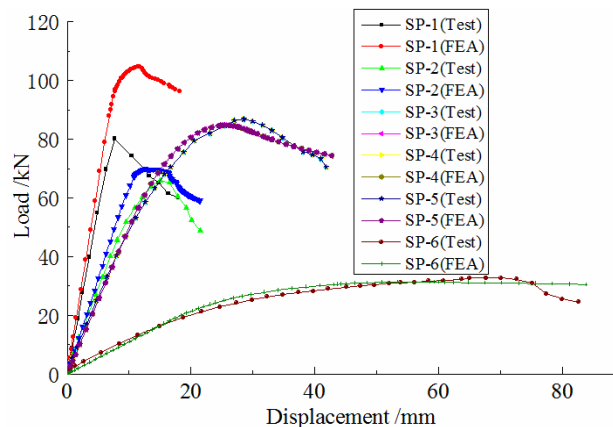


Fig. 6 Comparison of major axis bending experimental with FE results of load–displacement curves results

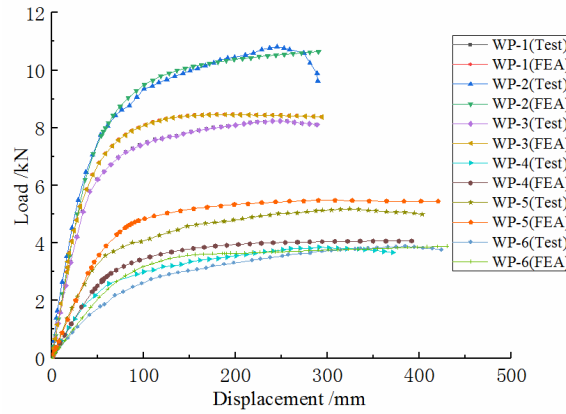


Fig. 7 Comparison of weak axis bending experimental results with FE results of load–displacement curves

4.3 Ultimate bearing capacity

Table 1 compares the ultimate loads generated by the FE model to those obtained from the experiments of the major axis bending specimen. Good agreement was obtained: except SP-1, the average ratio of the FE predicted load capacity to the experimentally measured load capacity was 0.96 with a standard deviation of 0.0668. A larger difference between the experimental and numerical results can be observed for SP-1. The main reason is that SP-1 was the first experimental specimen, with the maximum cross section height and also the biggest difficulty of experiment. Besides, the loading rate was too fast during experiment, so that it's a failure to capture the ultimate bearing capacity data, leading to a low ultimate bearing capacity result.

Table 2 compares the ultimate loads generated by the FE model to those obtained from the experiments of the major axis bending specimen. Good agreement was obtained: the average ratio of the FE predicted load capacity to the experimentally measured load capacity was 0.96 with a standard deviation of 0.0847.

It was concluded that the FE model is capable of accurately predicting the ultimate load, the failure mode, and the deformational behaviour of lipped C-section stainless steel beams, indicating that the model is able to accurately account for the mechanism of local buckling.

5 Finite Element Modelling

5.1 Simplified finite element model

It is quite complicated to build angel steels and the constraint between angle steels and component under the flange. Also, it is a long time needed in calculation and not applicable to parametric analysis. Therefore, three different geometric models were built to study the influence of angle steels on the local buckling bearing capacity of major axis bending specimens. First, angel steels are according to the actual size built on the model. Second, without building angel steels, angel steels and component under the flange are connected by Link Constraints in MPC, as shown in Fig. 8. Third, angel steels are removed without any link between two components under the flange. As to examine the effect of the initial defect amplitude, six analysis models and four different initial defect amplitudes were used according to the above geometric model and different defect conditions.

The experimental results and calculation results of simplified constrain analysis model are compared. Angel steels have effects only on the initial stiffness of specimens and the remove of angel steels will reduce the initial stiffness, but angle steels have almost no effect on ultimate bearing capacity so that it is not necessary to consider the impact of angle steels. Therefore, it is no problem to use simplified model without angle steel in following analysis of local buckling bearing capacity of lipped C-section stainless steel member.

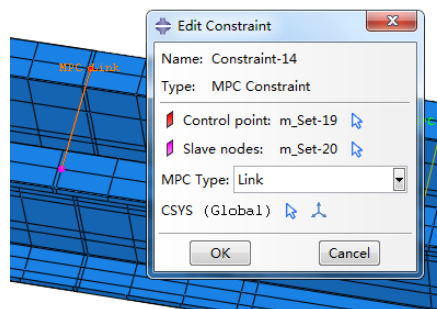


Fig. 8 Simplified constraint of angel steels of major axis bending specimen.

5.2 Simplified finite element model

As there are great quantity of links between upper flange of lipped C-section specimens and profiled sheet, the FE model is complex and the calculation is time-consuming and not easy to converge. The FE model used to parametric studies is not feasible. Therefore it is necessary to further simplify above simplified model.

Since the failure of the major axis bending specimens is mainly concentrated in the range of twice the local buckling half-wavelength, it is considered that only the pure bending section (simplified specimen) model within the range of mid-span without profiled sheet can be selected to analyse. The end constraints of simplified specimen can be simplified using rigid and hinged constraints, as shown in Figs. 9 (a) and (b). At the same time, to consider the influence of the length of pure bending section (simplified specimen), the length of pure bending section of 2.5 times the local buckling half-wavelength and that of third local buckling half-wavelength were added to make a comparative analysis.

The results of length simplified model were compared with those of original FE analysis model. As concluded, the model with the pure bending section of 2.5 times the local buckling half-wavelength is in good agreement with original FE model, which can simulate the mechanical performance of the major axis bending specimen. Therefore, this FE model is used to analyse parametric analysis.

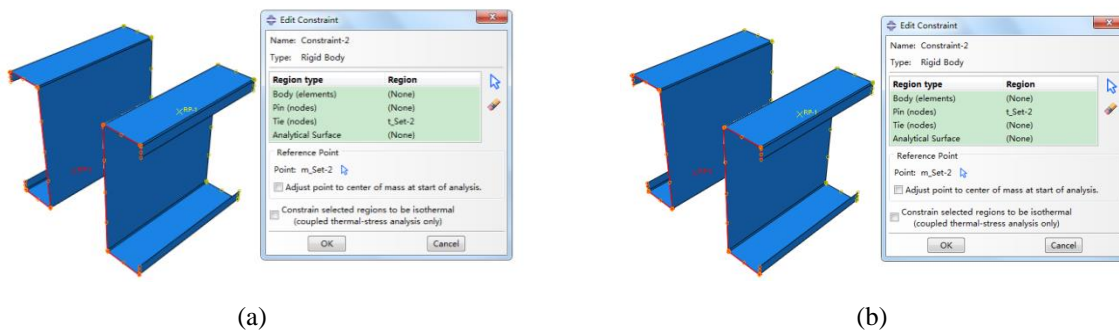


Fig. 9 Setting constraint of simplified length model of major axis bending specimen (a) pinned support and (b) fixed support.

5.3 Simplified imperfection model of weak axis bending beam

To investigate the influence of initial imperfection amplitude, four kinds of models were set up according to FE geometric model and different imperfection conditions of weak axis bending specimen. There are four different imperfection amplitudes, namely, no initial imperfections, the measured amplitude of the local imperfection, imperfection corresponding to 25% and 75% of initial imperfection cumulative distribution function, respectively. The experimental and simplified FE model load vs. displacement curves for weak axis bending specimen are compared. There are little differences among the results of four simplified FE model. A conclusion can be drawn that imperfection amplitude has little effect on ultimate bearing capacity.

5.4 Simplified length model of weak axis bending beam

The building and calculating of weak axis bending FE model is simple. But in order to get a FE model which can be applied to different cross-section under different test conditions, it is necessary to simplify the length of specimen. Finally, the simplified model only has to do with cross-section of specimen. Similar to the simplified process of major axis bending model, the length of pure bending section is chosen to be 1800mm, and the length of pure bending section is 2.0 times, 2.5 times and 3.0 times the local buckling half-wavelength for comparative analysis. To consider the influence of end constrains, the end of specimen is compared with two kinds of constraints, namely, rigid and pinned, as shown in Figs. 10 (a) and (b).

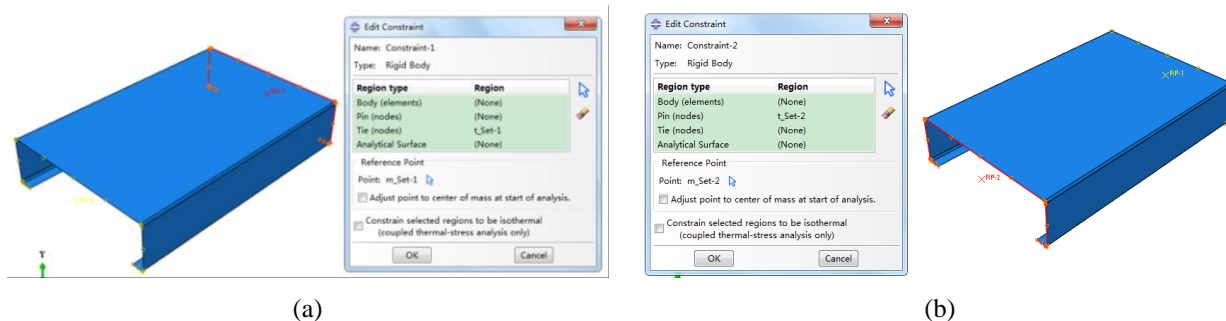


Fig. 10 Setting constraint of simplified length model of weak axis bending specimen (a) Pinned support and (b) fixed support

Comparing the finite element results of the simplified model with the test results in terms of failure modes, bending moment-curvature curve and local buckling bearing capacity, conclusions can be drawn that the FE model that the pure bending length is equal to 2.5 times the local buckling half-wavelength can better simulate the mechanical properties of weak axis bend specimen.

6 Parametric Studies

To increase the amount of available data pertaining to local buckling of lipped C-section stainless steel beams, the FE model was used in parametric studies.

6.1 Effect of mechanical properties

To investigate the effect of the property on the local buckling of lipped C-section stainless steel bending specimens, the specimens with the section of $C250 \times 75 \times 20$ are selected, the thickness include 0.8, 1.0, 1.2, 1.5, 1.8, 2.0, 2.5, 3.0, 3.5, 4.0, 5.0 and 6.0 mm, and the inner diameter of specimen is 2.0 mm. A total of 60 FE models were used to analyse the mechanical properties of five different materials, without considering the material hardening of corner section in the analysis. The finite element modelling parameters of each group are shown in Table 3. $H \times b \times a$ in the table shows the web height \times flange width \times lipped width, and t is the thickness of the specimen.

Table 3 Mechanical properties and amplitude of the initial geometric imperfections.

Group number	Section code $h \times b \times a / \text{mm} \times \text{mm} \times \text{mm}$	yield strength ($\sigma_{0.2} / \text{Mpa}$)	Material strengthening index (n)	Mode of initial geometric imperfection	Amplitude of the initial geometric imperfections
G1	C250 \times 75 \times 20	300	4	The first buckling mode (Local buckling)	0.14 t
G 2	C250 \times 75 \times 20	400	4	The first buckling mode (Local buckling)	0.14 t
G 3	C250 \times 75 \times 20	500	4	The first buckling mode (Local buckling)	0.14 t
G 4	C250 \times 75 \times 20	300	6	The first buckling mode (Local buckling)	0.14 t
G 5	C250 \times 75 \times 20	300	8	The first buckling mode (Local buckling)	0.14 t

The ultimate capacities and cross-sectional slenderness can be obtained from the parametric studies. The cross-sectional slenderness λ_l is defined as

$$\lambda_l = \sqrt{\frac{\sigma_{0.2}}{\sigma_{cr1}}} \quad (1)$$

where $\sigma_{0.2}$ is 0.2% proof stress, and σ_{cr1} is the elastic critical buckling stress.

Fig. 11 (a) displays the curves of the ratio of local buckling bearing capacity to full cross section yield bearing strength vs. nominal yield strength $\sigma_{0.2}$ on major axis bending specimen, and Fig. 11 (b) displays the curves of the ratio of local buckling bearing capacity to full cross section yield bearing strength vs. coefficient n . M_{nl} is the local buckling bearing capacity of specimen, and M_y is the full section yield bearing capacity of specimen.

Fig. 11 (a) indicates that, when the local buckling slenderness λ_l is small, the ratio of local buckling bearing capacity to full cross section yield bearing capacity M_{nl}/M_y increases with the nominal yield strength $\sigma_{0.2}$. When λ_l is larger, M_{nl}/M_y decreases with the increase of nominal yield strength $\sigma_{0.2}$. In general, the nominal yield strength $\sigma_{0.2}$ has little effect on M_{nl}/M_y and the three curves are close to each other. Fig. 11 (b) indicates that M_{nl}/M_y decreases with the increase of the hardening coefficient n . With the increase of the local buckling slenderness ratio λ_l , the three curves tend to coincide with each other, and M_{nl}/M_y tends to constant with the hardening coefficient n .

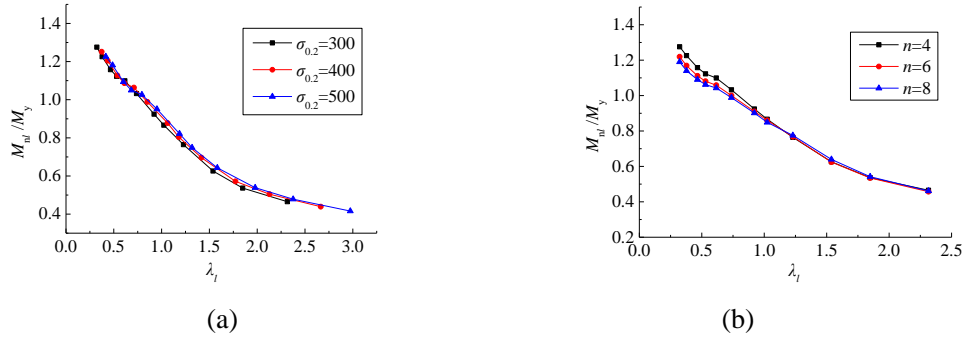


Fig. 11 Effect of mechanical property on the capacity of column specimen under major axis bending (a) Nominal yield stress, and (b) Strain hardening index n.

Figs. 12 (a) and (b) are the curves of the ratio of local buckling bearing capacity to full cross section yield bearing strength of weak axis bending specimen vs. local buckling slenderness λ_1 under different conditions of the material nominal yield strength $\sigma_{0.2}$ and the strain hardening coefficient n , respectively.

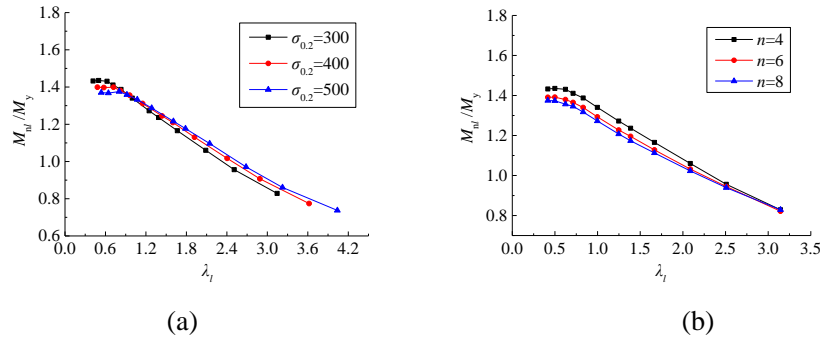


Fig. 12 Effect of mechanical property on the capacity of column specimen under weak axis bending (a) Nominal yield stress, and (b) Strain hardening index n.

Fig. 12 (a) shows that: (1) when the local buckling slenderness ratio λ_1 is small, the ratio of local buckling bearing capacity to full cross section yield bearing capacity M_{ni}/M_y decreases with the increase of nominal yield strength $\sigma_{0.2}$. When λ_1 is large, M_{ni}/M_y increases with the nominal yield strength $\sigma_{0.2}$. (2) In general, the nominal yield strength $\sigma_{0.2}$ has little effect on M_{ni}/M_y , but the effect is larger than that of major axis. Fig. 12 (b) shows that: (1) the ratio of local buckling bearing capacity to full-section yield bearing capacity M_{ni}/M_y decreases with the increase of the hardening coefficient n . (2) With the increase of the local buckling slenderness ratio λ_1 , the three curves tend to coincide with each other, and M_{ni}/M_y tends to constant with the hardening coefficient n .

6.2 Effects of mechanical properties in corner regions

To investigate the influence of the mechanical properties in corner regions on the local buckling bearing capacity of lipped C-section, the specimens with the section of C200 × 75 × 20 are selected, the thickness include 0.8, 1.0, 1.2, 1.5, 1.8, 2.0, 2.5, 3.0, 3.5, 4.0, 5.0 and 6.0 mm, and the inner diameter of specimen is 2.0 mm. Fig 13 presents the relation curve of the relative increase capacity ratios $\Delta M/M_1$ and the corner zone area proportion A_c/A , where A_c is the cross section corner zone, M_1 is the local buckling bearing capacity without considering the strength of corner zone material, M_2 is the local buckling bearing capacity considering the material hardening in the corner, ΔM is the increase value of local buckling bearing capacity, $\Delta M = M_2 - M_1$.

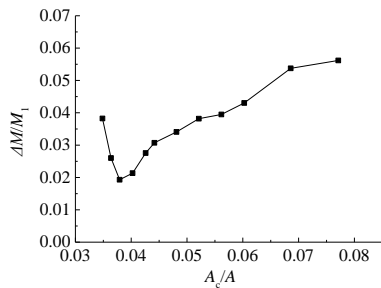


Fig. 13 $\Delta M/M_1$ - A_c/A curve (major axis bending)

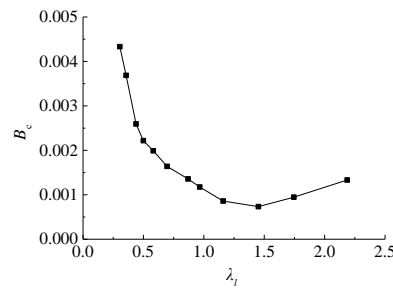


Fig. 14 B_c - λ_1 curve (major axis bending)

Fig. 13 shows that when A_c/A is less than 0.38, the relative increase value of bearing capacity $\Delta M/M_1$ decreases with the increase of the corner area proportion A_c/A . When A_c/A is more than 0.38, the relative increase value of bearing capacity $\Delta M/M_1$ increases with the corner area proportion A_c/A .

To further investigate the law of the contribution of the material hardening in corner to the increase of local buckling bearing capacity changing with the change of local slenderness ratio λ_1 , the method in the Technical Guide (2012) is used. The corner area enhancement index B_c can be calculated according to Eq. (2). The corner area enhancement index can better reflect the contribution of the increase of corner zone material strength per unit area to the increase of local buckling bearing capacity.

$$B_c = \frac{\Delta M}{M_1} \times \frac{A_c}{A} = \frac{M_c^c - M_c^f}{M_c^f} = \frac{\sigma_c^c - \sigma_c^f}{\sigma_c^f} \times \frac{A_c}{A} \approx \frac{\sigma^c - \sigma^f}{\sigma^f} \times \left(\frac{A_c}{A}\right)^2 \quad (2)$$

where M_c^c is the bearing capacity of corner, M_c^f is the bearing capacity of plate, σ_c^c is the full-section average stress considering the material hardening of corner, and σ_c^f is the full-section average stress without considering the material hardening of plate.

It can be seen from Eq. (2) that the corner enhancement index B_c is approximately equal to the product of the increase percentage of material hardening in the corner and the square of the area ratio of corner area when reaching the ultimate bearing capacity. Considering the increase of material hardening in the corner, the local buckling bearing capacity of lipped C-section stainless steel specimen is increased, and the contribution of the material hardening in the corner per unit area to the increase of bearing capacity decreases first and then increases with the increase of slenderness.

Through FE simulation analysis, the local buckling bearing capacities of two groups of weak axis bending specimens are obtained, and the relation curve between increase value of bearing capacity $\Delta M/M_1$ and the corner zone area proportion A_c/A are detailed in Fig. 15. Fig. 16 presents the relation curve between the corner area enhancement index B_c to the local slenderness ratio λ_1 , which can be observed that the contribution of the increase of material hardening in the corner to the increase of bearing capacity decreases with the increase of local slenderness ratio λ_1 , and the decreasing speed gradually decreases.

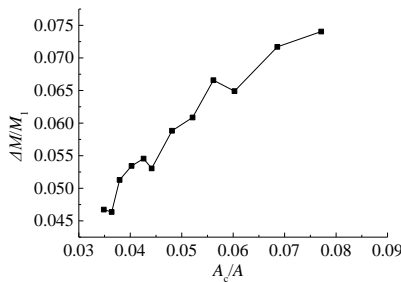


Fig. 13 $\Delta M/M_1$ - A_c/A curve (weak axis bending)

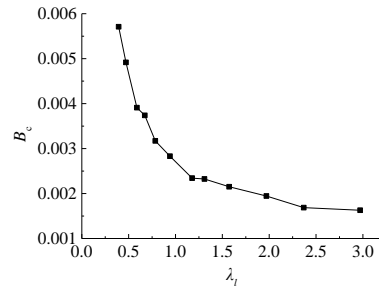


Fig. 14 B_c - λ_1 curve (weak axis bending)

6.3 Effect of amplitude of the initial geometric imperfections

Maintaining the initial geometry of the modal unchanged, the accurate finite element models for selected specimen groups were established with only the change amplitude of imperfection. In the FE model, the amplitude of introduced initial geometric imperfections is based on the cumulative distribution function (1998) of maximum imperfection, respectively, when the P ($\Delta < d$) is 0.25, 0.50, 0.75, 0.95 and 0.99. That is, the imperfection values are 0.14t, 0.34t, 0.66t, 1.35t and 3.87t, respectively. T is the thickness of specimen, and α is the amplitude coefficient of imperfection. Considering the direction of amplitude of imperfection, the imperfection values take -0.66t, -1.35t and -3.87t respectively, and the negative sign indicates that the imperfection direction is opposite to that of the first order mode. A total of eight kinds of amplitude of imperfection were selected. Test Plate material properties were used in the corner and plate area, respectively, and the initial imperfection distribution mode of the first order was adopted.

Fig. 17 presents the relation curves between the imperfection amplitude coefficients α and the bearing capacity. The dotted line in the figure is the calculation result when the imperfection direction is opposite to that of the first order mode.

It can be seen from Fig. 17 that: (1) the local buckling failure occurs in every specimen. The local buckling bearing capacity decreases with the increase of the initial geometric amplitude of imperfection and the decrease rate decreases with the increase of α ; (2) If the imperfection direction is opposite to that of the first order mode, the bearing capacity may decrease or increase, but the effect is very small; (3) The first-order buckling mode of SP 2 C250 \times 75 \times 20 \times 2.0 is two buckling half waves, as shown in Fig. 18 (a), which is symmetrical along the centre of the section, so that the buckling mode is exactly the same as the original mode when the imperfection direction is opposite to the first-order mode, meaning that the local buckling bearing capacity is the same. The first-order buckling modes of the two other groups of specimens are three buckling half-waves, as shown in Figs. 18 (b) and (c), and the buckling modes is different when the imperfection direction is opposite to the first-order mode, so that the local buckling bearing capacity is different.

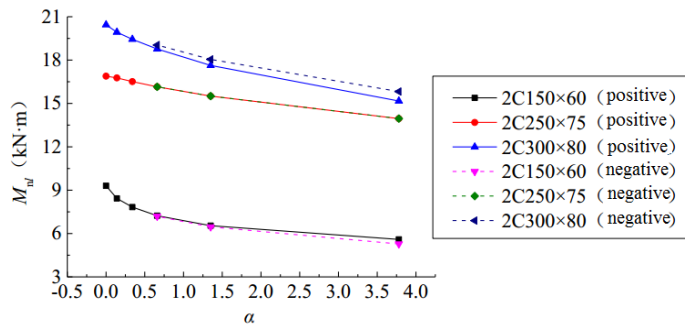


Fig. 17 Effect of amplitude of the geometric imperfection on the capacity of specimen under major axis bending

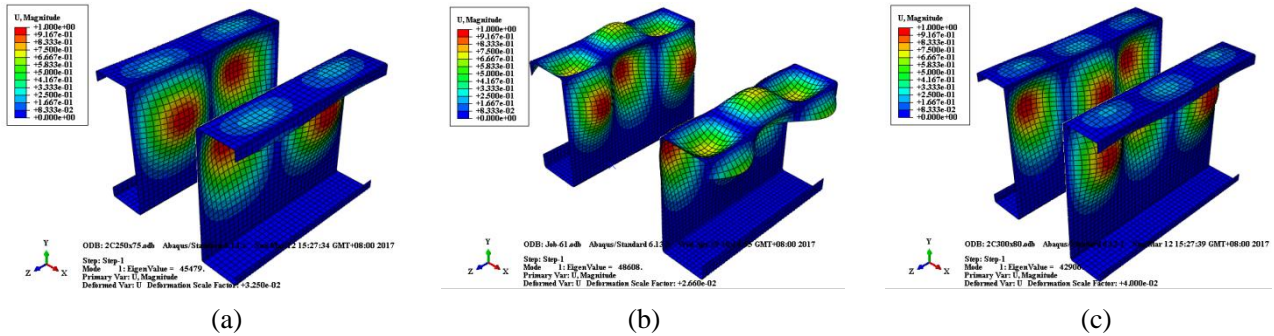


Fig. 18 Buckling modes of the first order of major axis bending beam (a) 2 C250x75x20x2.0, (b) 2 C150x60x20x2.0 and (c) 2 C300x80x20x2.0.

Fig. 19 presents the relation curves between the bearing capacities from FE analysis and the imperfection amplitude coefficient α of weak axis bending specimen. The dotted line in the figure is the calculation results of the opposite imperfection direction of the first order mode.

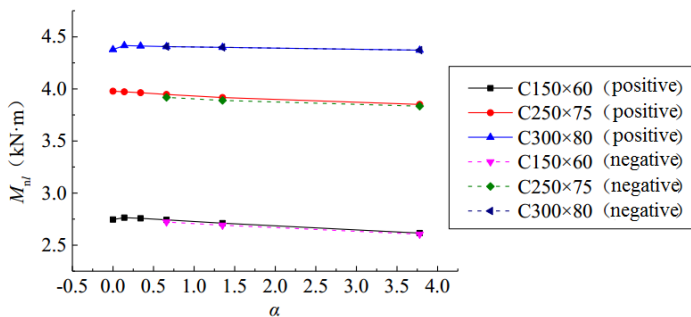


Fig. 19 Effect of amplitude of the geometric imperfection on the capacity of weak axis bending specimen.

Fig. 20 indicates that the local buckling failure occurs in every weak axis bending specimen. When initial geometric imperfection is small, the bearing capacity may be larger than that of the imperfection-free specimen. The bearing capacity decreases with the increase of the initial geometric imperfection amplitude. On the whole, the initial geometric imperfection has little imperfection on the bearing capacity. The maximum bearing capacities have only a difference of 3.62%. When the imperfection direction is opposite to that of the first order mode, the bearing capacity may reduce or maintain. The first-order buckling modes of specimen $C300 \times 80 \times 20 \times 2.0$ are two buckling half-waves anti-symmetry to the centre of the section, as shown in Fig. 20 (a). The buckling mode is exactly the same as the original modal, so that the bearing capacity is the same. The first buckling modes of the two other specimens are three buckling half-waves and not symmetrical along the centre of the section, as shown in Figs. 20 (b) and (c), so the bearing capacity is different.

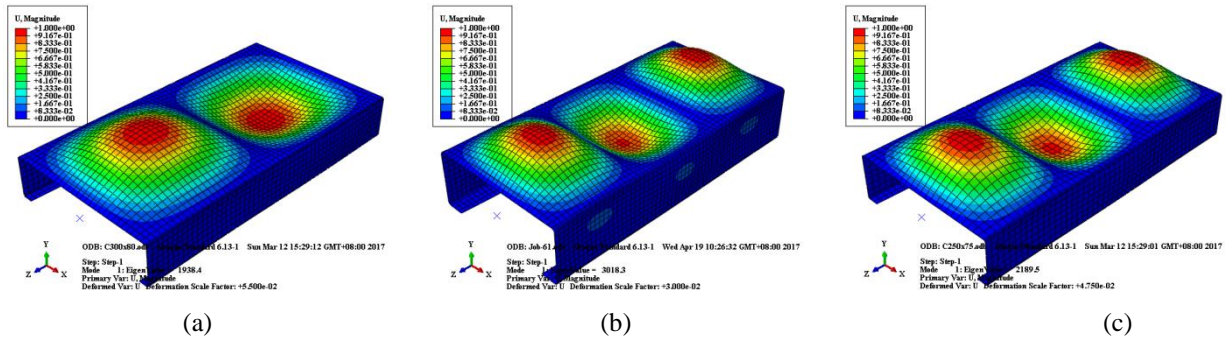


Fig. 20 Buckling modes of the first order of weak axis bending beam (a) C300×80×20×2.0, (b) C150×60×20×2.0 and (c) C250×75×20×2.0.

6.4 Effect of mode of the initial geometric imperfections

To get first ten order buckling modes, cold-formed stainless steel members of lipped C-section are selected, with section sizes including C150 × 60 × 20 × 2.0, C250 × 75 × 30 × 2.0 and C300 × 80 × 20 × 2.0. Maintaining the mechanical properties, the initial geometric imperfection amplitude and distribution direction, only the shapes of imperfection are changed. Flat and corner material properties are in accordance with the test of flat and corner area, respectively. Initial imperfection amplitude is value that the cumulative distribution function of maximum imperfection $P(\Delta < d)$ is 0.25, that is, the imperfection amplitude is 0.14t, and t is the thickness of the cross section. The imperfection direction is the same as the modal direction.

The major axis bending buckling analysis of three kinds of cross-section specimens was carried out. Each order model distribution characteristic is shown in Table 5.

Table 5 Model distribution of major axis bending specimen.

Section code $h \times b \times a \times t / \text{mm} \times \text{mm} \times \text{mm}$	Features of buckling mode				
	First order	Second order	Third order	Fourth order	Fifth order
2C150×60×20×2.0	3 half-waves positive symmetric	3 half-waves anti-symmetry	2 half-waves positive symmetric	2 half-waves anti-symmetry	4 half-waves positive symmetric
2C250×75×20×2.0	2 half-waves positive symmetric	2 half-waves anti-symmetry	3 half-waves positive symmetric	3 half-waves anti-symmetry	4 half-waves positive symmetric
2C300×80×20×2.0	3 half-waves positive symmetric	3 half-waves anti-symmetry	2 half-waves positive symmetric	2 half-waves anti-symmetry	4 half-waves positive symmetric
Section code $h \times b \times a \times t / \text{mm} \times \text{mm} \times \text{mm}$	Features of buckling mode				
	Sixth order	Seventh order	Eighth order	Ninth order	Tenth order
2C150×60×20×2.0	4 half-waves anti-symmetry	5 half-waves positive symmetric	5 half-waves anti-symmetry	5 half-waves positive symmetric	5 half-waves anti-symmetry
2C250×75×20×2.0	4 half-waves anti-symmetry	5 half-waves positive symmetric	5 half-waves anti-symmetry	5 half-waves positive symmetric	5 half-waves anti-symmetry
2C300×80×20×2.0	4 half-waves anti-symmetry	5 half-waves positive symmetric	5 half-waves anti-symmetry	5 half-waves positive symmetric	5 half-waves anti-symmetry

The top ten order modes of three kinds of specimens are local buckling. Among them, buckling modal distribution of specimens 2 C150 × 60 × 20 × 2.0 and 2 C300 × 80 × 20 × 2.0 are the same. The first four order distribution model of specimen 2 C250 × 75 × 20 × 2.0 are overall same as those of the other two groups, only the modal order is different. To this end, the first 1, 2, 3, 4, 7 and 8 order modes of each group of specimen are selected for bearing capacity analysis. The selected modes are shown in Figs. 21 (a) to (f). As an example, Fig. 21 shows the buckling mode of specimen 2 C250 × 75 × 20 × 2.0.

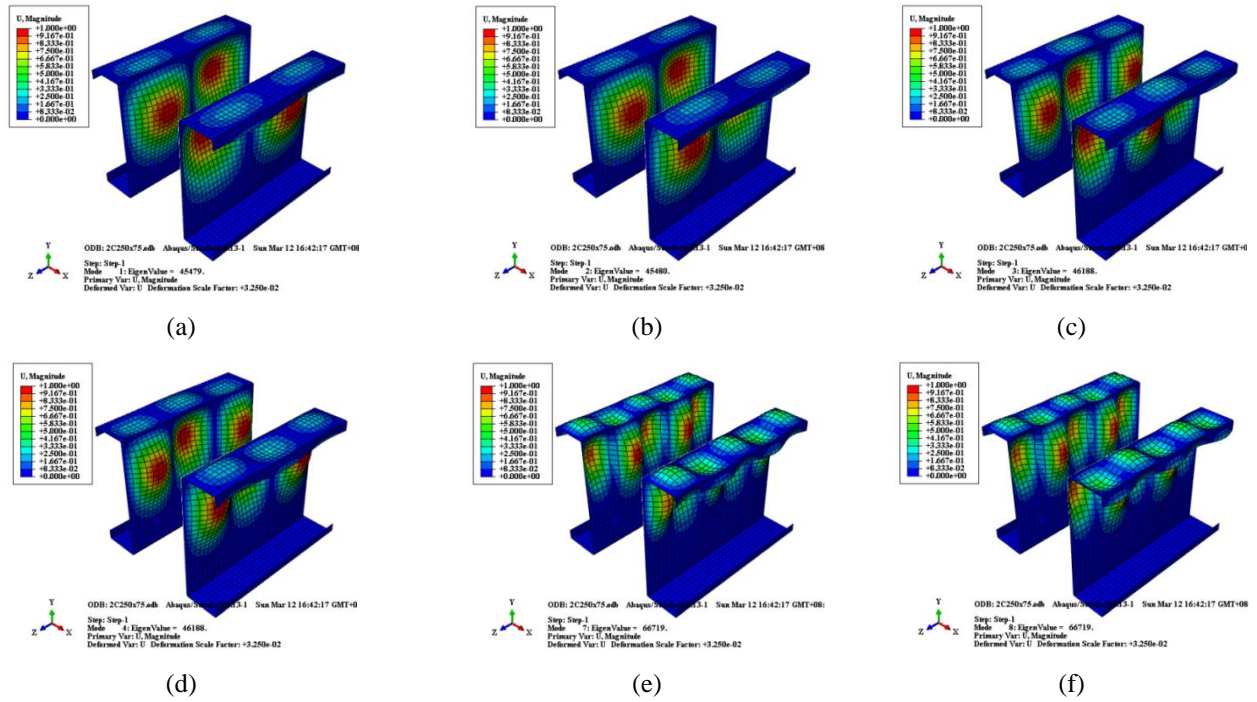


Fig. 21 Selected buckling mode of specimen 2C250×75×20×2.0 (a) first order, (b) second order, (c) third order, (d) fourth order, (e) seventh order and (f) eighth order.

The results of the finite element analyses are summarised in Table 6 for the local buckling tests

Table 6 Bearing capacities of major axis bending specimen under different buckling modes.

Section code $h \times b \times a \times t / \text{mm} \times \text{mm} \times \text{mm}$	Bearing capacities under different buckling modes $M_{nl} / \text{kN}\cdot\text{m}$						Failure mode
	First order	Second order	Third order	Fourth order	Seventh order	Eighth order	
2C150×60×20×2.0	8.43	8.41	8.80	8.80	8.49	8.46	Local buckling
2C250×75×20×2.0	16.77	16.77	16.26	16.20	16.35	16.37	Local buckling
2C300×80×20×2.0	19.94	19.97	20.72	20.72	20.01	20.17	Local buckling

It can be seen from Table 6 that, when introducing different initial imperfections of different buckling modes, the bearing capacities of major axis bending specimens are not much different, with the maximum bearing capacity and the minimum bearing capacity are not more than 5%. When the buckling mode is a symmetrical and anti-symmetrical buckling mode with two buckling half-waves, the bearing capacity is constant. When the buckling mode is the imperfection mode with buckling half-wave number of the same, or a symmetrical and anti-symmetrical buckling mode, the bearing capacity is almost the same. Therefore, in FE calculation, it is reasonable to consider the initial defect distribution model with only the introduction of the first order buckling mode.

The weak bending buckling analysis of three kinds of cross-section specimens was carried out to get first ten order buckling modes. Each order model distribution characteristic is shown in Table 7.

Table 7 Model distribution of weak axis bending specimen.

Section code $h \times b \times a \times t / \text{mm} \times \text{mm} \times \text{mm}$	Features of buckling mode				
	First order	Second order	Third order	Fourth order	Fifth order
C150×60×20×2.0	3 half-waves	2 half-waves	4 half-waves	5 half-waves	6 half-waves
C250×75×20×2.0	3 half-waves	2 half-waves	4 half-waves	5 half-waves	6 half-waves
C300×80×20×2.0	2 half-waves	3 half-waves	4 half-waves	5 half-waves	1 half-wave
Section code $h \times b \times a \times t / \text{mm} \times \text{mm} \times \text{mm}$	Features of buckling mode				
	Sixth order	Seventh order	Eighth order	Ninth order	Tenth order
C150×60×20×2.0	1 half-wave	7 half-waves	2×4 half-waves	2×5 half-waves	8 half-waves
C250×75×20×2.0	1 half-waves	7 half-waves	2×4 half-waves	2×5 half-waves	8 half-waves
C300×80×20×2.0	6 half-waves	7 half-waves	2×4 half-waves	2×5 half-waves	2×3 half-waves

The top ten order buckling modes of three kinds of specimens are local buckling. Among them, the buckling modal distribution of specimens $C150 \times 60 \times 20 \times 2.0$ and $C250 \times 75 \times 20 \times 2.0$ are the same. The first nine order distribution model of SP $C300 \times 80 \times 20 \times 2.0$ are the same as those of the other two groups, only the modal order is different. To this end, the first 1, 2, 3, 5, 6 and 8 order modes of each group of specimen were selected for buckling bearing capacity analysis. As an example, Fig. 22 shows the selected buckling mode of specimen $C250 \times 75 \times 20 \times 2.0$.

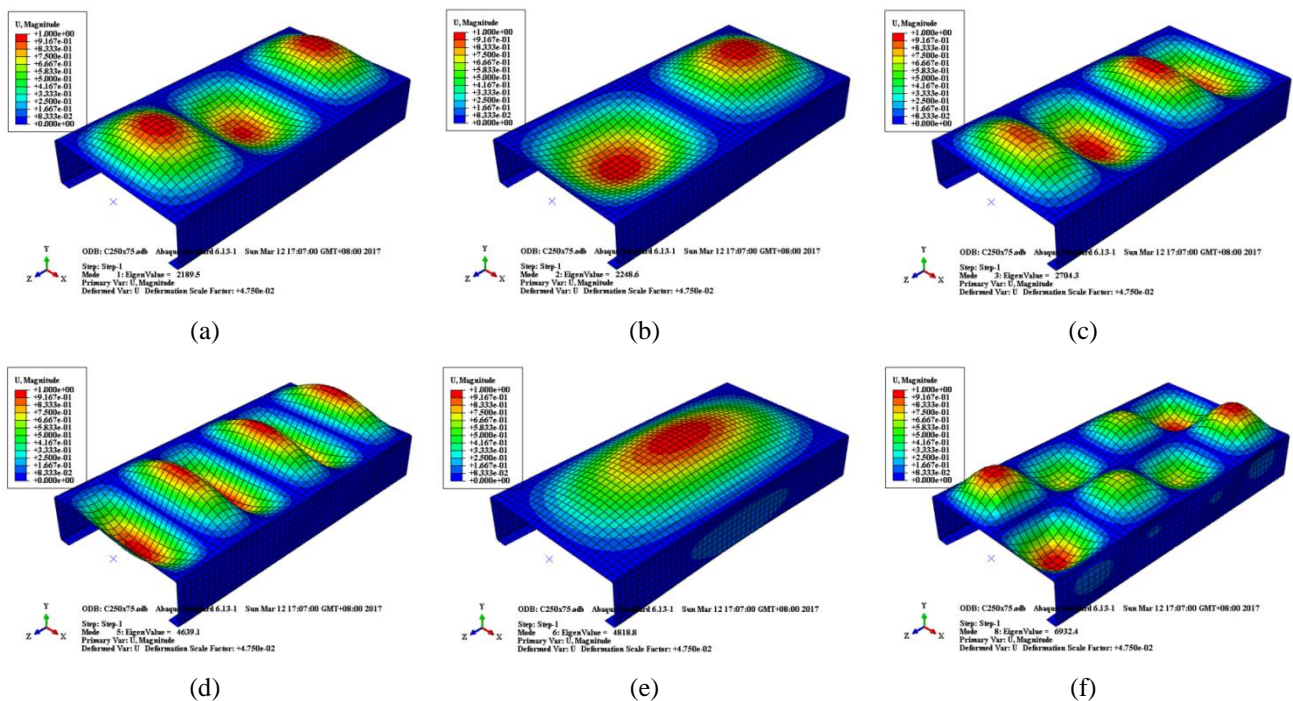


Fig. 22 Selected buckling mode of specimen $C250 \times 75 \times 20 \times 2.0$ (a) first order, (b) second order, (c) third order, (d) fifth order, (e) sixth order and (f) eighth order.

For the weak axis bending specimens under the six buckling modes, the local buckling bearing capacity obtained by finite element analysis are shown in Table 8. Table 8 indicates that the local buckling capacity in different order modes of the weak axis bending specimen is almost invariable, and the maximum bearing capacity and the minimum bearing capacity are not more than 1.5%.

Table 8 Bearing capacity in different order modes of weak axis bending specimen.

Section code $h \times b \times a \times t / \text{mm} \times \text{mm} \times \text{mm} \times \text{mm}$	Local buckling bearing capacity in different order modes ($M_{nl} / \text{kN}\cdot\text{m}$)						
	First order	Second order	Third order	Fifth order	Sixth order	Eighth order	Buckling mode
C150×60×20×2.0	2.764	2.776	2.745	2.738	2.745	2.746	Local buckling
C250×75×20×2.0	3.972	3.979	3.965	3.939	3.978	3.978	Local buckling
C300×80×20×2.0	4.416	4.411	4.417	4.378	4.377	4.378	Local buckling

6.5 Effect of section height-width ratio

To study the influence of the cross section aspect ratio on the local buckling bearing capacity of lipped C-section bending specimens, Sections with the same height and different width were selected for FE bearing capacity analysis. According to the statistical analysis, in the lipped C-section from Technical Specification for Stainless Steel Structures CECS 410:2015) [2015], the aspect ratio h/b (the ratio of web height to flange width) is between 2.0 to 3.0. In the lipped C-section from SFIA (Steel Framing Industry Association, aspect ratio is between 1.2 to 8.0. Taking into account the actual common cross-section aspect ratio, three kinds of cross-section bending specimens $C250 \times 50 \times 20$, $C250 \times 75 \times 20$ and $C250 \times 125 \times 20$ are finally selected, with the cross-section aspect ratio were 5.00, 3.33 and 2.00 and the radius of corner is 2.0mm. A series of different cross-section aspect ratios are obtained by varying the thickness of cross section, namely 0.8, 1.0, 1.2, 1.5, 1.8, 2.0, 2.5, 3.0, 3.5, 4.0, 5.0 and 6.0 mm, respectively.

Fig. 23 represents the relation curves between the ratios of the bearing capacity to the full cross section yield bearing capacity of major axis bending specimens under different aspect ratio conditions and slenderness ratio λ_1 .

Fig. 23 indicates that the variety of cross-section aspect ratio h/b has great influence on the buckling bearing capacity of major axis bending specimen under the condition of other parameters as the same. The ratio M_{nl}/M_y of the bearing capacity to the full cross section yield bearing capacity increases with the cross-section aspect ratio h/b . Therefore, the cross-section aspect ratio is an important factor affecting the bearing capacity of major axis bending beam.

Fig. 24 represents the relation curves between the ratios of the bearing capacity to the full cross section yield bearing capacity of weak axis bending specimens under different aspect ratio conditions and slenderness ratio λ_1 .

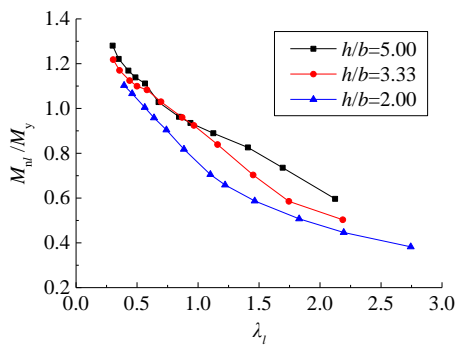


Fig. 23 Effect of section height-width ratio on bearing capacity of major axis bending specimens

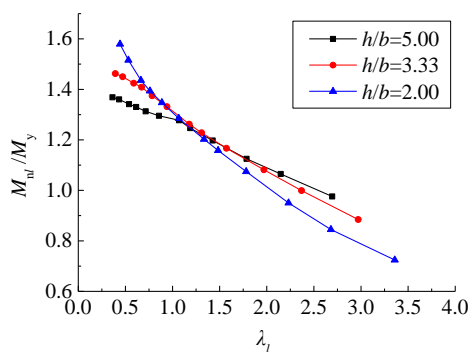


Fig. 24 Effect of section height-width ratio on bearing capacity of weak axis bending specimens.

Fig. 24 indicates that the variety of cross-section aspect ratio h/b has great influence on the bearing capacity of weak axis bending beams under the condition of other parameters as the same. When section length ratio is relatively small, the ratio M_{nl}/M_y of the bearing capacity to the full cross section yield bearing capacity decreases with the increase of the cross-section aspect ratio h/b . When section length ratio is relatively large, M_{nl}/M_y increases with the cross-section aspect ratio. M_{nl}/M_y is close to a straight line with the increase of the section length ratio λ_l . The smaller the cross-section aspect ratio, the faster M_{nl}/M_y decreases with the increase of the cross-section aspect ratio. Therefore, the cross-section aspect ratio is an important factor affecting the bearing capacity of weak axis bending beams.

7 Bearing Capacity Formula

Based on the parametric analysis above, further study is conducted on the main influential factors on the capacity of a beam, and the direct strength method is applied to establish the calculation equation of the capacity of a lipped C-section stainless steel beam. The calculation results are compared with the test results to verify the accuracy of the equation.

7.1 Simplified finite element model

Based on the direct strength method (DSM) in North American Specification (NAS), the direct strength method equation of a stainless steel beam of lipped C-section is assumed to be as follows.

$$M_{nl} = \begin{cases} M_y & \lambda_l \leq \lambda_{lim} \\ \frac{1}{\lambda_l^c} M_y \left(a - \frac{b}{\lambda_l^c} \right) & \lambda_l > \lambda_{lim} \end{cases} \quad (3)$$

where M_y is the full-section yield bearing capacity of specimen, $M_y = W\sigma_{0.2}$, W is the cross section resistance, λ_l is the local buckling slenderness ratio of specimen, $M_y = \sqrt{M_y/M_{crl}}$, M_{crl} is the component elastic buckling critical load, and a , b , c and λ_{lim} are the parameters to be determined.

7.2 Equation fitting

(1) Direct strength method of major axis bending beam

To determine the undetermined coefficients in Eq. (3), the finite element analysis is performed on 238 lipped C-section major axis bending stainless steel beams to calculate the capacity M_{nl} . The section type, thickness and specimen number are detailed in Table 1. For the specimens with a certain section, different section slenderness λ_l are generated by verify the section thickness t .

After data processing, a set of data for the section slenderness λ_l and the capacity M_{nl} of 238 major axis bending specimens were available for equation fitting, which is realized using the software Datafit in the reference of Eq. (3). Using the coefficients $a = 0.93$, $b = 0.13$ and $c = 0.57$ obtained from fitting. The maximum value of the function is $M_y = 1.66$, $\lambda_{lim} = 0.107$, for safety, $\lambda_{lim} = 0.10$ is selected. The following direct strength equation for calculating the capacity M_{nl} of major axis bending beams is established.

$$M_{nl} = \begin{cases} 1.66M_y & \lambda_l \leq 0.10 \\ \frac{1}{\lambda_l^{0.57}} M_y \left(0.93 - \frac{0.13}{\lambda_l^{0.57}} \right) & \lambda_l > 0.10 \end{cases} \quad (4)$$

The corresponding curves according to Eq. (4) and the direct strength method curve of North American Specification are plotted, as shown in Fig. 25. Comparing with the curves and data points in Fig. 25, it can be seen that: (1) when the cross section slenderness ratio λ_l is small, the calculation results of Eq. (4) are slightly lower than those of the North American Specification formula; (2) when the cross section slenderness ratio λ_l is large, the curve of Eq. (4) is located above the curve of the North American Specification. (3) The calculated point of major axis bending specimen distribute on both sides of Eq. (4), indicating the accuracy of the fitting formula.

(2) Direct strength method of weak axis bending beam

After data processing, a set of data for the section slenderness λ_l and the capacity M_{nl} of 229 weak axis bending specimens were available for equation fitting, which is realized using the software Datafit in the reference of Eq. (3). Using the coefficients $a = 1.71$, $b = 0.48$, $c = 0.45$ and $\lambda_{lim} = 0.28$ obtained from fitting, the following direct strength equation for calculating the capacity M_{nl} of weak axis bending beams is established.

$$M_{nl} = \begin{cases} 1.52M_y & \lambda_l \leq 0.28 \\ \frac{1}{\lambda_l^c} M_y \left(1.71 - \frac{0.48}{\lambda_l^{0.45}} \right) & \lambda_l > 0.28 \end{cases} \quad (4)$$

Fig. 26 represents a comparison of the direct strength in North American Specification, fitting equation Eq. (5) and numerical strengths. The curve of the fitting Eq. (5) is located above the curve of the North American Specification, indicating that the calculated values are too conservative. The calculated point of weak axis bending specimen distribute on both sides of the fitting Eq. (5), indicating the accuracy of the fitting formula.

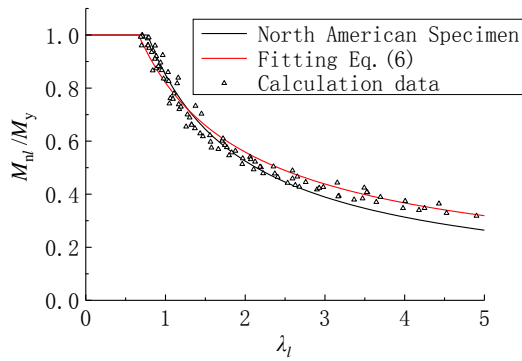


Fig. 25 Comparing of the direct strength equation with the numerical strength of weak axis bending specimen

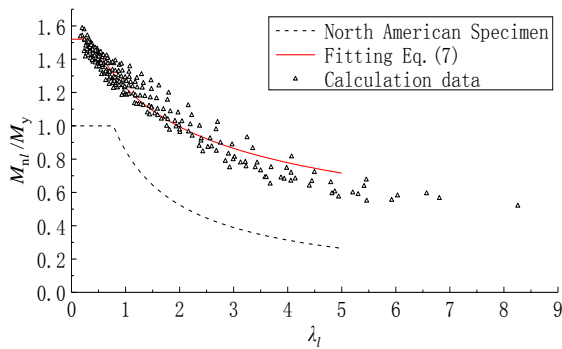


Fig. 26 Comparing of the direct strength equation with the numerical strength of major axis bending specimen

7.3 Comparison of the fitting equation with the test results

The results of the direct strength equation Eq. (4) was calibrated against the test results. The capacity of major axis bending beams calculated using the Eq. (4) and the test results are presents in the Table 9. The Table indicates that the calculation results fit well with the test results, with a standard deviation of 0.003 and mean of M_{cal}/M_T of 0.96, which verifies the accuracy of Eq. (4). The results of North American Specification formula are in better agreement with the experimental results, but not safe. M_{AISI} is the experimental value of local buckling bearing capacity, and DEVT is the deviation from the calculated value and the test value.

The results of the direct strength equation Eq. (5) was calibrated against the test results. The capacity of weak axis bending beams calculated using the Eq. (5) and the test results are presents in the Table 10. The Table indicates that the calculation results fit well with the test results, with a standard deviation of 0.009 and mean of M_{cal}/M_T of 1.01, which verifies the accuracy of Eq. (5). The results of North American Specification formula are too conservative.

Table 9 Fitting equation strength and test strength of major axis bending specimens.

Specimen code	Specimen number	λ_f	Test result $M_T/kN\cdot m$	North American Specification (AISI S100-07)			Fitting formula		
				$M_{AISI}/kN\cdot m$	DEV_T	M_{AISI}/M_T	$M_{cal}/kN\cdot m$	DEV_T	M_{cal}/M_T
SP-1	MB-1-A	1.53	18.02	20.84	15.59%	1.16	21.29	18.10%	1.18
	MB-1-B	1.52	18.02	21.09	16.99%	1.17	21.53	19.44%	1.19
SP-2	MB-2-A	1.16	14.82	16.08	8.54%	1.09	15.56	5.02%	1.05
	MB-2-B	1.14	14.82	16.39	10.59%	1.11	15.81	6.67%	1.07
SP-3	MB-3-A	0.76	19.52	20.18	3.38%	1.03	18.31	-6.19%	0.94
	MB-3-B	0.76	19.52	20.27	3.85%	1.04	18.43	-5.60%	0.94
SP-4	MB-4-A	0.95	13.59	14.12	3.84%	1.04	13.17	-3.10%	0.97
	MB-4-B	0.96	13.59	13.85	1.91%	1.02	12.95	-4.76%	0.95
SP-5	MB-5-A	0.94	11.67	11.29	-3.20%	0.97	10.51	-9.94%	0.90
	MB-5-B	0.94	11.67	11.26	-3.51%	0.96	10.48	-10.13%	0.90
SP-6	MB-6-A	0.63	7.38	7.04	-4.61%	0.95	6.96	-5.66%	0.94
	MB-6-B	0.64	7.38	6.94	-6.02%	0.94	6.81	-7.73%	0.92
				Average	1.48%	1.01	Average	-4.14%	0.96
				Standard deviation	0.003		Standard deviation	0.003	

Note: The average test value is the average of the calculation values without counting MB-1-A and MB-1-B. Since SP-1 is the first specimen in the test with the maximum cross-section and the test is also the most difficult with a too fast process loading rate, so the test failed to capture the ultimate bearing capacity of the real data, leading to a lower bearing capacity.

Table 10 Fitting equation strength and test strength of weak axis bending specimens.

Specimen code	Section code	λ_f	Test result $M_T/kN\cdot m$	North American Specification (AISI S100-07)			Fitting formula		
				$M_{AISI}/kN\cdot m$	DEV_T	M_{AISI}/M_T	$M_{cal}/kN\cdot m$	DEV_T	M_{cal}/M_T
WP-1	C100x50x20x2.0	0.66	1.75	1.25	-28.35%	0.72	1.71	-2.16%	0.98
WP-2	C150x60x20x2.0	0.97	2.33	1.91	-17.86%	0.82	2.74	17.59%	1.18
WP-3	C250x50x20x2.0	1.19	1.73	1.19	-31.04%	0.69	1.85	6.56%	1.07
WP-4	C250x75x20x2.0	1.33	3.43	2.00	-41.59%	0.58	3.23	-5.69%	0.94
WP-5	C250x75x20x2.5	1.02	4.86	3.08	-36.73%	0.63	4.49	-7.79%	0.92
WP-6	C300x80x20x2.0	1.47	3.71	2.12	-42.69%	0.57	3.57	-3.70%	0.96
				Average	-33.04%	0.67	Average	0.80%	1.01
				Standard deviation		0.009	Standard deviation		0.009

8 Conclusions

For AISI304 stainless steel, this paper performs finite element numerical simulation, parametric analysis and theoretical analysis on the stainless steel lipped C-section beam. Comparing the design strengths and fitting equation strengths with the test strengths, the following conclusions can be drawn:

- The finite element analysis indicates that the finite element mode in this paper can simulate well the mechanical performance of a stainless steel beam. When applying accurate material mechanical property parameters, reasonable boundary conditions and appropriate imperfection distribution.
- By simplifying the finite element model and comparing the results of the simplified model with the actual finite element model, it is concluded that the model 2.5-2 can better simulate the failure mode and local buckling bearing capacity of lipped C-section stainless steel major and weak axis bending specimens, which can also be used for parametric analysis.
- Based on the parametric analysis on several key factors, which have an effect on the capacity of major and weak axis bending beam specimens, it can be observed that the yield strength, hardening index, the enhanced properties of the corner areas and the amplitude and distribution modes of initial geometric imperfections and the cross section aspect ratio all have effect on the capacity. The cross section aspect ratio has the greatest influence.
- Based on the finite element analysis of 238 beam specimens, the direct strength equations for the major-axis bending capacity of lipped C-section stainless steel beam is fitted. The direct strength equations for the weak-axis bending capacity of lipped C-section stainless steel beam is fitted, Based on the finite element analysis of 229 beam specimens. The fitting equations are verified against the test results.

References

- [1] Kwon Y B, Hancock G J. Tests of cold-formed channels with local and distortional buckling [J]. *Journal of Structural Engineering*, 1992, 118(7): 1786-1803.
- [2] Feng Z, Young B. Experimental investigation of cold-formed high-strength stainless steel tubular members subjected to combined bending and web crippling [J]. *Journal of Structural Engineering*, 2007, 133(7):1027-1034.
- [3] Feng Z, Young B. Cold -formed high -strength stainless steel tubular sections subjected to web crippling [J]. *Journal of Structural Engineering*, 2007, 133(3): 368-377.
- [4] Feng Z, Young B. Cold - formed stainless steel sections subjected to web crippling [J]. *Journal of Structural Engineering*, 2006, 132(1): 134-144.
- [5] Niu S, Rasmussen K J R, Asce M, Feng F. Local–global interaction buckling of stainless steel I-beams. I: Experimental investigation [J]. *Journal of Structural Engineering*, 04014194.
- [6] Niu S, Rasmussen K J R, Asce M, Feng F. Local–global interaction buckling of stainless steel I-beams. II: Numerical study and design [J]. *Journal of Structural Engineering*, 04014195.
- [7] Liu Fang. Theoretical and Experimental Investigations on the Method of Effective Section of Stainless Steel Lipped C Stub Columns [D]. Thesis (Master) Nanjing: School of Civil Engineering, Southeast University, 2015.
- [8] Zhang Yang. Performance research on local buckling and distortional buckling of cold-formed thin-wall C-section steel flexural members [D]. Chongqing University, 2014.
- [9] Yuan Huanxin. Local and Local-Overall Buckling Behaviour of Welded Stainless Steel Members under Axial Compression [D]. Tsinghua University, 2014.
- [10] Hancock G J, Kwon Y B, Bernard ES. Strength design curves for thin-walled sections undergoing distortional buckling [J]. *Journal of Constructional Steel Research*, 1994, 31(2–3):169–86.
- [11] Schafer B W. Review: the direct strength method of cold-formed steel member design [J]. *Journal of constructional steel research*, 2008, 64(7): 766-778.
- [12] Schafer B W, Grigoriu M, Peköz T. A probabilistic examination of the ultimate strength of cold-formed steel elements [J]. *Thin-Walled Structures* 31 (1998) 271-288.
- [13] Schafer B W. *Direct Strength Method design guide*. Washington (DC): American Iron and Steel Institute; 2006. 171 pages.
- [14] Gardner L. A new approach to stainless steel structural design [D]. PhD Thesis. Department of Civil and

Environmental Engineering, Imperial College, London, 2002.

- [15] Schafer B W, Peköz T. Computational modelling of cold-formed steel: characterizing geometric im-perfections and residual stresses [J]. *Journal of Constructional Steel Research*. 1998, 47(3): 193-210.
- [16] Cheng Y. Distortional buckling of cold-formed steel members in bending[R]. Research Report, American Iron and Steel Institute, Committee on Specifications, 2005.
- [17] Haidarali M R, Nethercot D A. Finite element modelling of cold-formed steel beams under local buckling or combined local/distortional buckling [J]. *Thin-Walled Structures*. 2011, 49(12): 1554-1562.
- [18] National Standard of the People's Republic of China. Technical Specification for Stainless Steel Structures (CECS 410:2015) [S]. Beijing, China Planning Press, 2015.
- [19] Technical Guide for Cold-Formed Steel Framing Products. Steel Framing Industry Association, 2012.